Journal of The Electrochemical Society, **159** (5) G62-G66 (2012)
0013-4651/2012/159(5)/G62/5/$28.00 © The Electrochemical Society

Enhanced Dielectric Permittivity of the $Bi_2Mg_{2/3}Nb_{4/3}O_7$-Bi Nano-Composite Amorphous Films Grown at Room Temperature

Hyun-June Jung,[a] Hyun-Ah Song,[a] Soon-Gil Yoon,[a,b,*,z] Chung-Soo Kim,[c] and Jeong-Yong Lee[c]

[a]School of Nano Science and Technology and [b]Graduate of Analytical Science and Technology, Chungnam National University, Daeduk Science Town, 305-764 Daejeon, Korea
[c]Department of Materials Science and Engineering, Korea Advanced Institute of Science and Technology, Yuseong-gu, 305-701 Daejeon, Korea

Bismuth metal nanocrystals were self-assembled into the $Bi_2Mg_{2/3}Nb_{4/3}O_7$ (BMNO) dielectric films at room temperature by radio-frequency sputtering for percolative BMNO-Bi nano-composite films. For capacitor applications, BMNO-Bi nano-composite amorphous films sandwiched between protective Al_2O_3 layers showed an enhanced dielectric permittivity of ~220 maintaining an authentic leakage current characteristics, compared with the dielectric permittivity of about 50 observed in the BMNO amorphous films. Moverover, room-temperature grown BMNO-Bi nano-composite films sandwiched between the BMNO protection layers exhibited a high dielectric permittivity of about 310. Enhanced dielectric permittivity of the BMNO-Bi nano-composite films was attributed to a hybrid model that included a space-charge polarization, a dipolar response, and nano-capacitors. The BMNO-Bi composite films exhibiting an enhanced dielectric permittivity can provide an epoch-making breakthrough for the flexible electronic device applications.
© 2012 The Electrochemical Society. [DOI: 10.1149/2.004206jes] All rights reserved.

Manuscript submitted January 2, 2012; revised manuscript received February 24, 2012. Published March 7, 2012.

The integration of electronic components on flexible polymer substrates will be critical to the development of future flexible micro and nanoelectronic systems. Many of these systems will involve devices based on oxide thin films. The integration of these components on structural flexible substrates will require the deposition of films with uniform composition and microstructure on large-area polymers with low-temperature processing and cost. In the case of organic thin-film transistors (OTFTs),[1–7] introduction of gate dielectrics having a high dielectric permittivity on polymer substrates for low-voltage operation and high yield would enable the development of a range of technologies including low-cost digital logic devices, electronic paper and books, wearable electronics, and flexible large-area displays.[8–10]

The dielectric behavior of ferroelectric-metal bulk composites has attracted much attention due to extraordinary dielectric enhancement.[11,12] These devices are ideal for use as a new type of ceramic capacitor when large charge-storage capacity is required over a wide range of voltages, temperatures, and frequencies. Metal nanocrystals self-assembled in dielectric thin films grown at room temperature were applied for flexible nano-floating gate memory (NFGM) devices.[13]As microsystems move toward faster speeds and miniaturization, the characteristics required of both the electronic components and the devices are continually changing. In particular, miniaturization is becoming increasingly important because more and more devices are being made portable. Thin films are also required for the size reduction of capacitor materials. In films, the dielectric permittivity of the dielectric material decreases with decreasing thickness. Accordingly, films with a high dielectric permittivity are in high demand and have been the focus of considerable research. Especially, capacitor applications that use thin films require a low leakage current density and a high dielectric permittivity. If thin film capacitors are required to be integrated onto flexible substrates, high-dielectric-permittivity oxide films are needed to be grown at room temperature. Generally, if the ferroelectric films having a high dielectric permittivity were grown at a room temperature, they show a low dielectric permittivity (below 10) because they are an amorphous structure. To obtain a high dielectric permittivity in the amorphous films, BMNO dielectric materials with a pyrochlore structure have been chosen and they have the dielectric permittivity of about 210 for the crystallized bulk material.[14] In the case of thin films, 200-nm-thick BMNO films deposited at room temperature showed a low leakage current density of about 10^{-8} A/cm^2 at 3 V and a dielectric permittivity of about 45 at 100 kHz.[15,16] A high dielectric permittivity of ~45 in the amorphous BMNO films grown at room temperature had not been observed even at many ferroelectric thin films. Because the BMNO thin films maintained an amorphous phase even at a high temperature above 900°C, they were reported to be useful for high-*k* gate dielectric applications.[17,18] However, because the dielectric permittivity of the BMNO films deposited at room temperature is still low, an new structure of the BMNO-Bi nano-composite was suggested and they have greater dielectric permittivity than the reported BMNO films.[19,20] However, they had not shown an enough dielectric permittivity for future electronic device applications and still showed a leakage problem at a high voltage.

Especially, for embedded capacitor applications, it is important to achieve a low leakage current density in the range of applied voltage as well as a high dielectric permittivity. In the present study, to guarantee the BMNO-Bi nano-composite films with a low leakage current density, Al_2O_3 protection layers, which are well-known for their good insulation properties, were applied to sandwich the BMNO-Bi nano-composite films. The Al_2O_3 protection films were grown at 180°C using atomic layer deposition (ALD). The deposition temperature can be decreased below 180°C for deposition on the flexible substrates.

For an achievement of both a higher dielectric permittivity and the simpler nano-composite preparation process than the Al_2O_3/BMNO-Bi nano-composite films/Al_2O_3 structures, BMNO/BMNO-Bi nano-composite films/BMNO structure using the ultra-thin BMNO protection layer of a high dielectric permittivity was also addressed, and their structure was consecutively ex situ prepared by variations in deposition atmosphere alone using an rf sputtering at room temperature. In the present study, dielectric and leakage properties of the Al_2O_3/BMNO-Bi/Al_2O_3 and the BMNO/BMNO-Bi/BMNO structures were addressed in detail.

Experimental

For Al_2O_3 protection layer at 180°C by atomic layer deposition, tri-methyl-aluminum (TMA, $(CH_3)_3Al$) and distilled water were used as precursors and reactant, respectively, with pulse time 0.1 s. The bubbler temperatures of TMA and distilled ionized (DI) water were maintained at 10°C, respectively, and a nitrogen (purity of 99.9999%) was used as both a carrier and a purge gas with purge time of 10 s. Copper electrodes were used because copper is less expensive than the other noble metals. The BMNO-Bi composite and the BMNO films were deposited by radio-frequency magnetron sputtering on

* Electrochemical Society Active Member.
[z] E-mail: sgyoon@cnu.ac.kr

Downloaded 24 May 2012 to 143.248.118.124. Redistribution subject to ECS license or copyright; see http://www.ecsdl.org/terms_use.jsp

Al_2O_3/Cu/Si substrates at room temperature. A BMNO ceramic disk 2 inches in diameter was used as a target and the rf-power was maintained at 40 W. The base and working pressures were 8×10^{-4} and 7×10^{-1} Pa, respectively. The BMNO-Bi composite films were grown ex situ in a pure argon atmosphere of 100 sccm (standard $cc \cdot min^{-1}$) using a single BMNO target, while the BMNO films were grown in an atmosphere made up of equal parts Ar (10 sccm) and O_2 (10 sccm). The deposition rates of the BMNO-Bi composite films and the BMNO films were 4.8 and 1.5 nm/min, respectively. The microstructure and chemical state of both films were investigated by high-resolution transmission electron microscope (HRTEM) and X-ray photoelectron spectroscopy (XPS), respectively. Self-assembled Bi nanocrystals in the amorphous BMNO films were clearly identified by X-ray diffraction (XRD) using a Cu kα radiation and a Ni filter. The oxygen vacancies existing in the BMNO-Bi composite films were identified by a measurement of the oxygen concentration in the BMNO-Bi and BMNO films using Auger electron spectroscopy (AES). For electrical measurement, Cu top electrodes with dimensions of $100 \times 100\ \mu m^2$ were exactly patterned by lift-off lithography and sputtered by direct current (dc) magnetron sputtering. The dielectric properties of the BMNO capacitors were evaluated at 100 kHz using an impedance gain phase analyzer (HP 4194A). The leakage current characteristics of the BMNO capacitors were investigated via HP4145B semiconductor parameter analysis.

Results and Discussion

Dielectric and the leakage properties of Al_2O_3/BMNO-Bi/Al_2O_3 structure were compared with those of Al_2O_3/BMNO/Al_2O_3 structures. The deposition rates of the BMNO-Bi composite films and the BMNO films were 4.8 and 1.5 nm/min, respectively. The thickness of the BMNO-Bi composite films was varied from 50 to 1000 nm, while that of the BMNO films was limited to 300 nm because their deposition rate was too low.

The root mean square (rms) roughness of the Al_2O_3 thin films grown on Cu/Si substrates at 180°C by atomic layer deposition was varied from 5 to 6 nm. Here, the rms roughness of the copper electrode grown on Si (001) substrates at room temperature by dc sputtering was approximately 0.6 nm. An abrupt increase of the roughness of the Al_2O_3 films by ALD was attributed to an increase of the roughness (about 3 to 4 nm) of the copper electrode by an oxidation of the copper electrode in oxygen atmosphere before deposition of the Al_2O_3 films at 180°C. Figures 1a and 1b show the variations in the dielectric permittivity (also capacitance density) and the leakage current density of the Al_2O_3 films of various thicknesses, respectively. As shown in Fig. 1a, the dielectric permittivity of the films increased slightly, i.e., from 6 to 8, with increasing thickness, while the capacitance density decreased linearly with increasing thickness. Although the dielectric permittivity of the oxide materials does not dependent on the thickness, their dielectric permittivity decreased with decreasing the film thickness below a critical thickness because the dead layer having a low dielectric permittivity was formed at an interface between the films and the bottom electrode. The dielectric permittivity of the Al_2O_3 thin films was almost approached to that of the Al_2O_3 bulk materials (~9). Figure 1b shows the leakage current density of the films for various thicknesses as a function of applied field. Leakage current density of the Al_2O_3 films decreased with increasing thickness. Thin film capacitors require a high dielectric permittivity and a low leakage current density. Thus, it is important to choose the optimal thickness of the Al_2O_3 protection layer. The 20-nm thick Al_2O_3 films showed both a high capacitance density and a low leakage current density although they did not show the highest capacitance density. Therefore, in the present study, 20-nm thick Al_2O_3 protection films were chosen to achieve a high dielectric permittivity and a low leakage current density. The dielectric loss (tan δ) of the Al_2O_3 films of various thicknesses (10–40 nm) was varied from 2 to 0.4%.

Possibility of the existence of the bismuth nanocrystals self-assembled in the BMNO for BMNO-Bi nano-composite films was presupposed by the thermodynamic equilibrium, as shown in Fig. 1c.

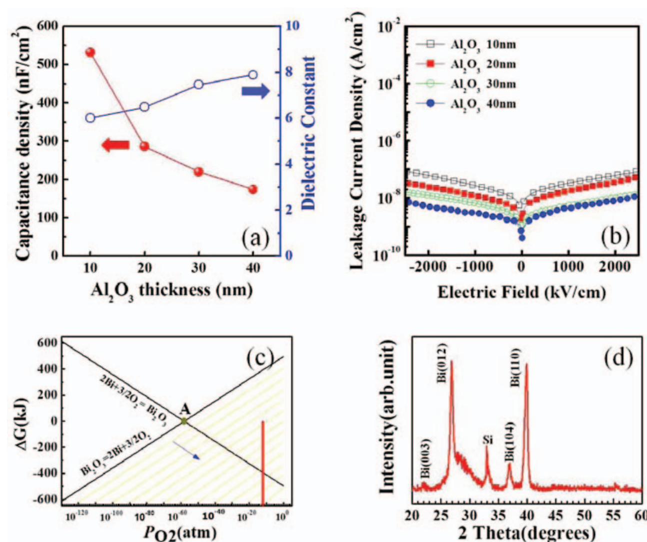

Figure 1. Variations in (a) capacitance density/dielectric permittivity at 100 kHz and (b) leakage current density vs. applied field for Al_2O_3 protection layers of various thicknesses. The capacitor structure was Cu/Al_2O_3/Cu/Ti/Si and a Ti buffer layer was used to improve the adhesion between Cu and Si. The dielectric loss of the Al_2O_3 films was about 0.7% at 100 kHz. (c) The thermodynamic expectation of metallic bismuth and bismuth oxide formation as a function of oxygen partial pressure. Solid lines show the relationship between Gibbs free energy and oxygen partial pressure at an equilibrium state. The yellow lines are plotted under the non-equilibrium state of an rf sputtering. The vertical line (red color) in the figure indicates an oxygen partial pressure in a pure argon ambient atmosphere. (d) X-ray diffraction pattern of 300-nm-thick Bi_2O_3 thin films grown by rf sputtering at room temperature in argon ambient.

Solid-lines (black color) exhibit the ΔG-P_{O2} relationship for the formation of bismuth oxide or bismuth metal at an equilibrium state. From the figure, oxygen partial pressure for the formation of bismuth metal by the reduction of bismuth oxide is below approximately 10^{-58} atm. However, in practice, because a sputtering process is performed under a non-equilibrium state in argon ambient alone, solid line exhibiting the stable state of bismuth metal in the figure should be moved into higher oxygen partial pressure (yellow colors) along the arrows (see Fig. 1c), if thermodynamic expectation is considered together with experimental conditions such as deposition temperature and rf power. Although the rf sputtering is performed without the substrate heating, the substrate temperature lays in the range of 50–80°C by a radiation of radio-frequency. The addition of the energies such as a temperature and radio frequency power during the deposition in a pure argon atmosphere effectively induces the reduction of the bismuth oxide. As a result, the region where the bismuth metal is stable is enlarged toward the higher oxygen partial pressure. Because an rf sputtering is performed in a pure argon ambient (purity of 99.9999%), the oxygen partial pressure in the case of Bi_2O_3 film deposition in the pure argon ambient is approximately 10^{-12} atm, which is indicated as a vertical dotted line (red color) in the figure. From the thermodynamic expectation including an experimental condition, the Bi_2O_3 deposition in argon ambient makes possible the existence of the bismuth nanocrystal within the Bi_2O_3 phase. Practically, to prove the thermodynamic speculation for the self-assembled Bi metal in Bi_2O_3 films, X-ray diffraction (XRD) analysis for 300-nm thick Bi_2O_3 films grown by rf sputtering at room temperature in a pure argon ambient was performed (see Fig. 1d). XRD pattern shows various peaks indicating the existence of Bi metal assembled in the Bi_2O_3 films, while a broad Bi_2O_3 peak was observed at $2\theta = 29°$, indicating an amorphous phase. This result proves that the thermodynamic expectation for self-assembled Bi nanocrystal can be equally applied for BMNO films grown at room temperature in argon ambient (will be discussed at Fig. 2).

Downloaded 24 May 2012 to 143.248.118.124. Redistribution subject to ECS license or copyright; see http://www.ecsdl.org/terms_use.jsp

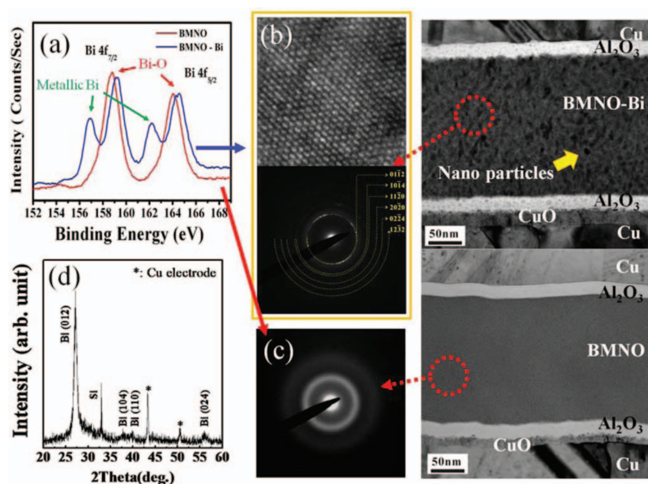

Figure 2. (a) XPS Bi 4f spectra of BMNO-Bi nano-composite films and BMNO films grown ex situ at room temperature by varying the sputtering atmosphere. The right figures in (b) and (c) are TEM cross-sectional images of Al_2O_3/BMNO-Bi nano-composite films/Al_2O_3/Cu and Al_2O_3/BMNO single-phase films/Al_2O_3/Cu structure, respectively. (b) HRTEM image (top) and selective area diffraction pattern (bottom) of bismuth nanocrystals. The spots in diffraction pattern were consistent with the XRD data of bismuth metal. (d) XRD pattern of 600-nm-thick BMNO-Bi nano-composite films (here, Cu peaks were due to the bottom and top electrodes).

BMNO-Bi nano-composite films were analyzed by XPS Bi 4f spectra, as shown in Fig. 2a. In addition, to visually investigate the BMNO-Bi nano-composite films, transmission electron microscopic analysis was also performed. Figures 2b and 2c show the TEM cross-sectional images of both the Cu/Al_2O_3/BMNO-Bi composite film (300 nm)/Al_2O_3/Cu and the Cu/Al_2O_3/BMNO film (300 nm)/Al_2O_3/Cu samples, respectively. From the cross-sectional images, BMNO-Bi nano-composite films exhibited a number of small particles immersed in the BMNO matrix, while the BMNO films showed a smooth and dense morphology without particles. Approximate 10-nm-thick interfacial layer between Al_2O_3 and Cu/Si was identified as copper oxide that formed as a result of oxidation during the deposition of Al_2O_3. Each layer was clearly evident in the TEM image, and the BMNO film was dense and uniform within the Al_2O_3 layers. A selective area diffraction pattern (SADP) observed in the circle of the image (Figure 2c) indicates that the BMNO film showed an amorphous structure. On the other hand, in the case of the BMNO-Bi nano-composite films, many nano-particles were observed in the amorphous BMNO matrix (from the image in the right side of Fig. 2b). High-resolution TEM image and a selective-area diffraction pattern (SADP) of the particles observed in the circles were shown in Fig. 2b. From the high resolution image, particles exhibit a clear crystalline structure with a mean size of 10–13 nm, and from the SADP pattern of the crystalline phase, the lattices observed from the each plan perfectly consist with the XRD data[21] of bismuth metal. The above results clearly show that the bismuth nanocrystals can be self-assembled in the BMNO films at room temperature. X-ray photoelectron spectroscopic analysis (Bi 4f spectra) revealed binding energies of $4f_{7/2}$ = 156.8 and $4f_{5/2}$ = 162.1 eV for bismuth metal, while those of $4f_{7/2}$ = 159.5 and $4f_{5/2}$ = 164.8 eV were attributed to a bismuth oxide phase when they were compared with the XPS handbook.[22] The BMNO-Bi nano-composite films showed a mixture of metallic bismuth and bismuth oxide phases, indicating a lower metallic bismuth concentration compared with that of bismuth oxide, while BMNO films consisted of a bismuth oxide phase only with no bismuth metal phase. The XPS profiles (not shown here) indicated that the elements Mg and Nb existed only as oxide phases in both the BMNO-Bi nano-composite and BMNO films.[20] In order to investigate the existence of the bismuth nanocrystals in the large area of the BMNO films, XRD pattern of

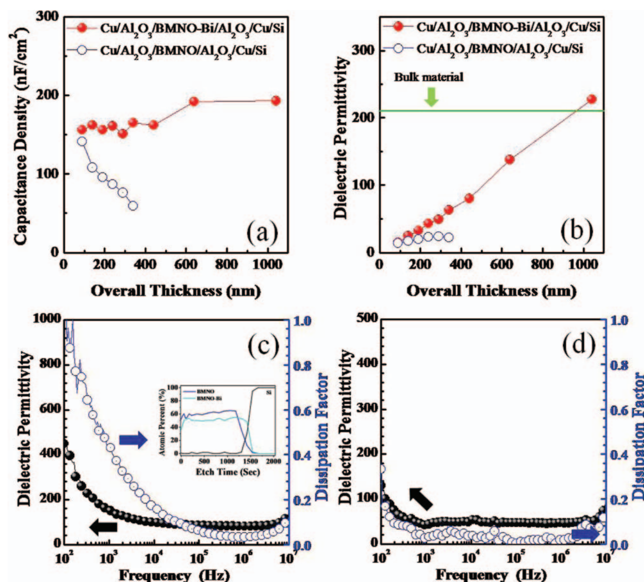

Figure 3. (a) Capacitance density and (b) dielectric permittivity as a function of overall thickness in Al_2O_3/BMNO-Bi composite films/Al_2O_3 and the Al_2O_3/BMNO/Al_2O_3 films. In (b), the horizontal dotted line indicates the dielectric permittivity (~210) of the BMNO crystallized bulk material. Variations in dielectric permittivity and the dissipation factor as a function of frequency in (c) Cu/200-nm-thick BMNO-Bi composite films/Al_2O_3/Cu and (d) Cu/Al_2O_3/200-nm-thick BMNO-Bi composite films/Al_2O_3/Cu capacitors. An inset of (c) shows the AES depth-profiles exhibiting oxygen concentrations in the BMNO-Bi and BMNO films. (d) Cu/Al_2O_3/200-nm-thick BMNO-Bi composite films/Al_2O_3/Cu capacitors. In (b), the horizontal dotted line indicates the dielectric permittivity (~210) of the BMNO crystallized bulk material.

the 600-nm thick BMNO-Bi nano-composite films was shown in Fig. 2d. The peaks consistent with that of bismuth metal were clearly observed at XRD patterns and no peaks characteristic of a BMNO phase were observed. Based on the Scherrer formula[23] and the θ-2θ XRD pattern, the mean size of the bismuth metal was ranged from 10–13 nm, which is consistent with the HRTEM image (see Fig. 4a).

The relationships between capacitance density and film thickness for the BMNO-Bi nano-composite and the BMNO films are shown in Fig. 3a. In the case of the BMNO films, capacitance density decreased linearly with increasing thickness. This result is a typical phenomenon observed in the dielectric materials. On the other hand, in the case of BMNO-Bi nano-composite films, capacitance density was maintained at about 160 nF/cm^2 as the film thickness increased. Generally, in dielectric materials, the capacitance density is inversely proportional to the film thickness when the dielectric materials have a permittivity dielectric permittivity regardless of thickness (capacitance (C) = $\varepsilon_0 \varepsilon_r \frac{A}{d}$, where ε_0 is vacuum permittivity, ε_r is the dielectric permittivity, A is the area, d is the film thickness). The constant capacitance density with increasing thickness for the BMNO-Bi nano-composite films suggests that the dielectric permittivity varies with thickness. The relationships between the dielectric permittivity and film thickness for the BMNO-Bi nano-composite and BMNO films are shown in Fig. 3b. The dielectric permittivity of the BMNO-Bi nano-composite films increased linearly with film thickness, while that of the BMNO films increased slightly at film thicknesses ranging from 50 to 300 nm, and was saturated as about 25 at film thicknesses greater than 200 nm. In BMNO films, the dielectric permittivity decreased below a critical point in thickness because the low-dielectric-permittivity layer that was formed between high-dielectric-permittivity BMNO materials and the bottom electrode dominantly influenced the overall dielectric permittivity by decreasing thickness.[24] However, the dielectric permittivity of the BMNO-Bi nano-composite films increased linearly with increasing film thickness with no critical point

Downloaded 24 May 2012 to 143.248.118.124. Redistribution subject to ECS license or copyright; see http://www.ecsdl.org/terms_use.jsp

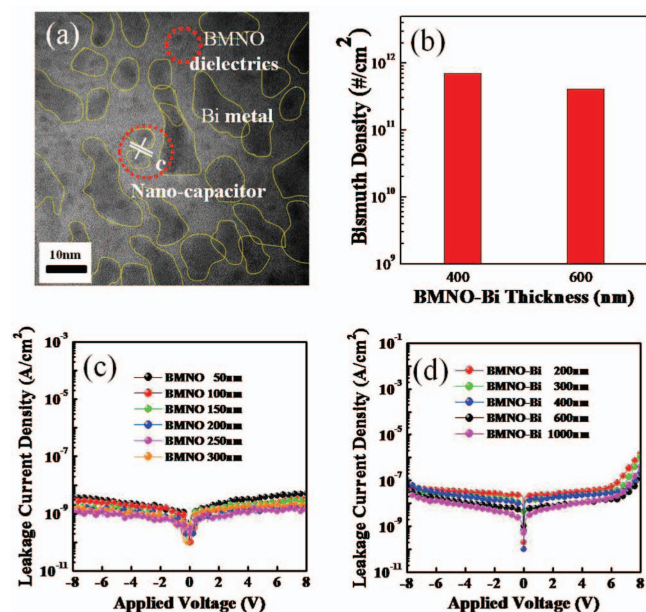

Figure 4. (a) High-resolution TEM image in 600-nm-thick BMNO-Bi nano-composite films and (b) Bismuth nanocrystal density (#/cm^2) in the BMNO-Bi composite films of 400 and 600 nm thickness. Variations in the leakage current density vs. applied voltage for different BMNO film thicknesses (c) in the Al_2O_3/BMNO/Al_2O_3 structure and for different BMNO-Bi composite film thicknesses (d) in the Al_2O_3/BMNO-Bi composite films/Al_2O_3 structure.

at which the dielectric permittivity reached a maximum. Thus, we sought to investigate the reason for this linear increase. The dielectric enhancement in the ferroelectric-metal composite bulk materials has been attributed to a decrease in the effective thickness of the dielectric layer and an increase in the effective electrode area.[25] Other researchers have hypothesized that space charge polarization contributes to the ultrahigh permittivity.[26] However, the reason for the enhanced dielectric permittivity is difficult to identify in the BMNO-Bi nano-composite films. An alternative explanation for the dielectric enhancement in the BMNO-Bi nano-composite films is a hybrid model that involves space charge polarization, the dipolar response of BMNO itself, and a nano-capacitor effect. This model has been suggested for percolative ferroelectric-metal composite bulk materials.[27] The contribution of the space charge polarization to the dielectric permittivity was clearly shown by the relationship between the dielectric permittivity and frequency in Cu/200-nm-thick BMNO-Bi nano-composite film/Al_2O_3/Cu capacitors without an Al_2O_3 top layer (see Fig. 3c). A sharp increase in both the dielectric permittivity and the dissipation factor in the range of frequency below 1 kHz was attributed to the space charges (for example: oxygen vacancy) existing in the nano-composite films formed by an argon atmosphere. Oxygen vacancies in the BMNO-Bi composite films were analogized by a deficient oxygen concentration through an AES depth-profile, compared with the stoichiometric oxygen concentration in the BMNO films (as shown in an inset of Fig. 3c). For the 200-nm-thick BMNO-Bi nano-composite films sandwiched at both side by Al_2O_3 (see Fig. 3d), the slight increase in the dielectric permittivity and the dissipation factor in the frequency range below 1 kHz suggests that a space charge polarization still contributes to the dielectric property. A hybrid model (contribution of the BMNO dielectric material and nano-capacitor) for enhancement of the dielectric permittivity in the 600-nm-thick BMNO-Bi composite films was clearly evident in the 75 nm × 75 nm size of HRTEM image (see Fig. 4a). In the image indicated by a circle "c", bismuth metals acted as top and bottom electrodes for nano-capacitors. As a result, the enhancement of the dielectric permittivity in the BMNO-Bi nano-composite films was attributed to the space charge polarization effect (Bi impurity and oxygen vacancy), the dipolar response (BMNO dielectrics itself), and the nano-capacitors (Bi/BMNO/Bi structure). Both the space charge polarization and the decreases in the effective thickness of the dielectric layer (the "nano-capacitor" effect) play important concurrent roles in the enhancement of the dielectric permittivity in the percolative composite.[27] The ultrahigh permittivity occurring at low frequency is mainly attributable to the space charge polarization. Due to the hybrid effect, the 1000-nm-thick BMNO-Bi nano-composite films showed a dielectric permittivity of about 220 and a dissipation factor of 2% at 100 kHz. The HRTEM images of the BMNO-Bi composite films with various thicknesses showed that the amount of bismuth metal in given area (bismuth density) was permittivity regardless of film thickness (see Fig. 4b). Thus, an increase in the film thickness increased the number of the nano-capacitors, which increased the dielectric permittivity of the BMNO-Bi nano-composite films.

Evaluation of current leakage behavior as well as of the dielectric properties is very important for capacitor applications that use BMNO-Bi composite films. Figures 4c and 4d show variations in the leakage current densities as a function of applied voltage in the BMNO films and the BMNO-Bi nano-composite films, respectively. As shown in Fig. 4c, the current leakage in the BMNO films of various thicknesses (50–300 nm) was varied from 1×10^{-9} to 5×10^{-9} A/cm^2 at an applied voltage of 8 V. The BMNO films sandwiched between Al_2O_3 films exhibited excellent leakage current characteristics, although the dielectric permittivity of the structure was low compared with BMNO films grown at room temperature without a protection layer.[28] On the other hand, BMNO-Bi nano-composite films showed higher leakage current densities than those of the BMNO films. However, the leakage current density was approximately 0.1 μA/cm^2 at ~8 V for all films (see Fig. 4d). For capacitor applications, leakage current density of the films was at least required to have below ~μA/cm^2, although it is dependent on the applied field and the film thickness.[29] Therefore, BMNO-Bi nano-composite films sandwiched by Al_2O_3 layers exhibited the excellent dielectric and leakage current properties for the film capacitor applications.

A low dielectric permittivity Al_2O_3 protection layer was changed to a high dielectric permittivity BMNO films for a nano-composite film to have a high dielectric permittivity. Both the BMNO-Bi nano-composite films and the BMNO protection layer were consecutively prepared ex situ at room temperature by variation in the deposition atmosphere alone using radio frequency magnetron sputtering.

Figures 5a and 5b showed variations in the capacitance density/dielectric permittivity at 100 kHz and the leakage current density for different BMNO protection layer thicknesses, respectively. As shown in Fig. 5a, the dielectric permittivity of the films was maintained in the range of 31–30 with increasing thickness from 40 to 80 nm, while the capacitance density decreased linearly with increasing thickness. The dielectric permittivity of the BMNO thin films showed an increase of about four times as high as that of the Al_2O_3 protection layer. Figure 5b shows the leakage current density of the films for various thicknesses as a function of applied voltage. The 40-nm thick BMNO films showed a low breakdown voltage of

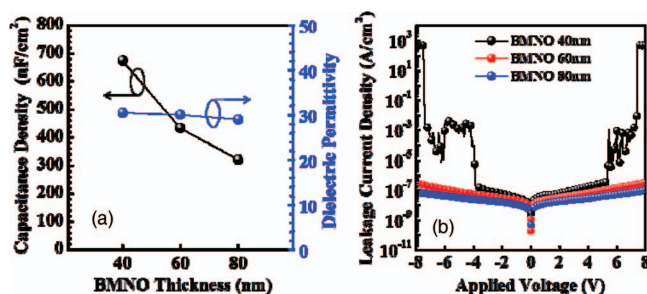

Figure 5. Variations in (a) capacitance density/dielectric permittivity at 100 kHz and (b) leakage current density vs. applied voltage for BMNO protection layers of various thicknesses.

Downloaded 24 May 2012 to 143.248.118.124. Redistribution subject to ECS license or copyright; see http://www.ecsdl.org/terms_use.jsp

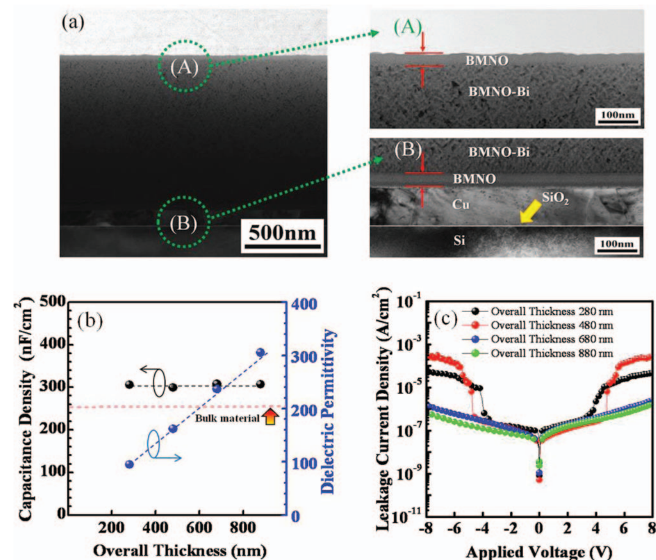

Figure 6. (a) TEM cross-sectional images of 40-nm-thick BMNO/BMNO-Bi composite films/40-nm-thick BMNO/Cu/Si structure. Here, right figures of (a) indicate the magnified images of interfacial layers in "A" and "B" of (a).Variations in the capacitance density and the dielectric permittivity at 100 kHz for (b) different overall thicknesses. (c) Relationship between leakage current density and applied voltage for different overall thicknesses in the BMNO/BMNO-Bi composite films/BMNO structure.

about 4 V, although they exhibited a low leakage current density of about 10^{-7} A/cm^2 below 4 V. The samples with a thickness greater than 60 nm showed a high breakdown voltage (~8 V) and a low leakage current density. In the present study, 40-nm thick BMNO protection films exhibiting the highest dielectric permittivity were chosen to achieve a high dielectric permittivity and a low leakage current density of the nano-composite films.

In Fig. 6a, the combined structure, 40-nm thick BMNO/600-nm thick BMNO-Bi nano-composite films/40-nm thick BMNO/Cu, was clearly observed by TEM cross-sectional images. The "A" and "B" in right side of Fig. 6a indicate the clear images in the BMNO protection layer/BMNO-Bi nano-composite film and BMNO-Bi nano-composite film/BMNO protection layer/Cu/Si structure, respectively. The 40-nm thick BMNO protection layer was identified to be an amorphous structure (electron diffraction pattern is not shown here), while BMNO-Bi nano-composite films were composed of bismuth nanocrystals assembled in the BMNO amorphous phase. The microstructure of the BMNO-Bi nano-composite films was not remarkably changed although the Al_2O_3 protection layer was replaced by BMNO protection layer.

The overall dielectric permittivity of the BMNO/BMNO-Bi nano-composite films/BMNO capacitors, which is shown in Fig. 6b, showed a similar thickness dependence on that of the composite films sandwiched by Al_2O_3 (Figs. 3a and 3b), while the 680-nm thick films exhibited a dielectric permittivity of ~240 larger than dielectric permittivity (~140) of 680-nm-thick Al_2O_3/BMNO-Bi/Al_2O_3 films. The 880-nm-thick films showed a dielectric permittivity of about 310 (at 100 kHz), which is higher than that (~210) of the 1040-nm-thick Al_2O_3/BMNO-Bi/Al_2O_3 films. The dissipation factors (tan δ) of all films were maintained at about 2 to 3%.

The overall leakage current density as a function of thickness in the BMNO/BMNO-Bi/BMNO capacitors was shown in Fig. 6c. The 280 and 480-nm-thick films exhibited a breakdown voltage of about 4 and 5 voltage, respectively. However, films of thicknesses above 680 nm showed the leakage current densities below ~μA/cm^2 at 8 V, indicating a stable leakage current behavior at a high applied voltage. From the results, BMNO as a protection layer of the BMNO-Bi nano-composite films played an important role in improvement of both the leakage current density and a dielectric permittivity.

Conclusions

Bismuth nanocrystals in BMNO films grown at room temperature were successfully self-assembled by variation in a sputtering atmosphere alone for percolative capacitors. The 1000-nm thick BMNO-Bi nano-composite films sandwiched between 40-nm-thick Al_2O_3 protection layers showed an enhanced dielectric permittivity of about 220, compared with that of the BMNO films (~50). Moreover, the 800-nm-thick BMNO-Bi nano-composite films sandwiched between 40-nm-thick BMNO protection layers exhibited a dielectric permittivity of about 310. The enhancement of the dielectric permittivity in the BMNO-Bi nano-composite films was attributed to a hybrid model that included space charge polarization, a dipolar response, and nano-capacitors.

Acknowledgments

This work was funded by KOSEF grant funded by the Ministry of the Economy, Science and Technology (MEST) (No. 2009-0079164, 2009-008146).

References

1. C. D. Dimitrakopoulos and P. R. L. Malenfant, *Adv. Mater. (Weinheim Ger.)*, **14**, 99 (2002).
2. J. Fraxedas, *Adv. Mater. (Weinheim Ger.)*, **14**, 1603 (2002).
3. M. Shtein, J. Mapel, J. B. Benziger, and S. R. Forrest, *Appl. Phys. Lett.*, **81**, 268 (2002).
4. D. Knipp, R. A. Street, A. Völkel, and J. Ho, *J. Appl. Phys.*, **93**, 347 (2003).
5. C. Bartic, H. Jansen, A. Campitelli, and S. Borghs, *Org. Electron.*, **3**, 65 (2002).
6. Y. Fujisaki, Y. Inoue, T. Kurika, S. Tokito, H. Fujikake, and H. Kikuchi, *Jpn. J. Appl. Phys., Part 1*, **43**, 372 (2004).
7. G. Wnag, D. Moss, A. J. Heeger, H. M. Zhang, M. Narashimhan, and R. E. Demaray, *J. Appl. Phys.*, **95**, 316 (2004).
8. G. Horowitz, *J. Mat. Res.*, **19**, 1946 (2004).
9. L. A. Majewski, M. Grell, S. D. Ogier, and J. Veres, *Org. Electron.*, **4**, 27 (2003).
10. M. Kitamura, T. Imada, and Y. Arakawa, *Appl. Phys. Lett.*, **83**, 3410 (2003).
11. C. Pecharromán, F. Esteban-Betegón, J. F. Bartolomé, S. López-Esteban, and J. S. Moya, *Adv. Mater.*, **13**, 1541 (2001).
12. Z. M. Dang, C. W. Nan, and D. Xie, *Appl. Phys. Lett.*, **85**, 97 (2004).
13. N. J. Seong, H. J. Jung, and S. G. Yoon, *Phys. Status Solidi A*, **208**, 932 (2011).
14. D. P. Cann, C. A. Randall, and T. R. Shrout, *Solid State Commun.*, **100**, 529 (1996).
15. J. H. Park, C. J. Xian, N. J. Seong, S. G. Yoon, S. H. Sohn, H. M. Chung, J. S. Moon, H. J. Jin, S. E. Lee, J. W. Lee, H. D. Kang, Y. K. Chung, and Y. S. Oh, *Appl. Phys. Lett.*, **89**, 232910 (2006).
16. C. J. Xian, J. H. Park, K. C. Ahn, S. G. Yoon, J. W. Lee, W. C. Kim, S. T. Lim, S. H. Sohn, J. S. Moon, H. M. Jung, S. E. Lee, I. H. Lee, and Y. K. Chung, *Appl. Phys. Lett.*, **90**, 052903 (2007).
17. B. S. Sahu, J. K. Ahn, C. J. Xian, S. G. Yoon, and P. Srivastava, *J. Phys. D: Appl. Phys.*, **41**, 135311 (2008).
18. B. S. Sahu, J. K. Ahn, N. J. Seong, and S. G. Yoon, *J. Appl. Phys.*, **102**, 054103 (2007).
19. N. D. Cuong, J. K. Ahn, K. W. Park, N. J. Seong, and S. G. Yoon, *Appl. Phys. Lett.*, **93**, 212901 (2008).
20. J. K. Ahn, N. D. Cuong, N. J. Seong, and S. G. Yoon, *J. Electrochem. Soc.*, **156**, G134 (2009).
21. *JDCPS-International Centre for Diffraction Data*, 1997, Card No. 85-1331.
22. J. F. Moulder, W. F. Stickle, P. E. Sobol, and K. D. Bomben, in *Handbook of X-ray Photoelectron Spectroscopy*, edited by J. Chatain (Perkin-Elmer, Eden Prairie, MN), 1992, Chap. 2, p. 191.
23. B. D. Cullity and S. R. Stock, *Elements of X-ray Diffraction*. 2001, Chap. 3, p. 170, Prentice-Hall, Englewood Cliffs.
24. C. J. Xian, J. H. Park, S. G. Yoon, J. S. Moon, S. T. Lim, S. H. Sohn, H. M. Jung, Y. N. Shin, and W. C. Kim, *J. Appl. Phys.*, **101**, 084114 (2007).
25. C. Pecharromán and J. S. Moya, *Adv. Mater.*, **12**, 294 (2000).
26. L. C. Costa, F. Henry, and M. A. Valente, *Eur. Polym. J.*, **38**, 1495 (2002).
27. Z. Chen, J. Huang, Q. Chen, C. Song, G. Han, W. Weng, and P. A. Du, *Scripta Materialia*, **57**, 921 (2007).
28. J. K. Ahn, N. D. Cuong, and S. G. Yoon, *J. Vac. Sci. Technol. B*, **26**, 1277 (2008).
29. W. J. Borland and S. Ferguson, Assembled passive components in printed wiring boards: A technology review. Circuit Tree, 2001, March, (2001).

Downloaded 24 May 2012 to 143.248.118.124. Redistribution subject to ECS license or copyright; see http://www.ecsdl.org/terms_use.jsp